crystals

MDPI

Article

Utilization of a CO_2 Storage Material: Shape-Controlled Preparation of $CaCO_3$ Microspheres

Xianlong Meng [1,2], Long Zhao [2], Haitao Guo [3], Feng Sha [2], Huihu Shi [2], Zhaojun Wu [2] and Jianbin Zhang [1,2,*]

1 Key Laboratory of Coal-based CO2 Capture and Geological Storage, China University of Mining and Technology, Xuzhou 221008, China
2 Inner Mongolia Engineering Research Center for CO2 Capture and Utilization, Hohhot 010051, China
3 Inner Mongolia Internet Information Office, Hohhot 010070, China
* Correspondence: tadzhang@pku.edu.cn; Tel.: +86-471-6575722; Fax: +86-471-6575722

Received: 30 July 2019; Accepted: 16 August 2019; Published: 20 August 2019

Abstract: Homogeneous $CaCO_3$ microspheres were controllably synthesized via a simple hydrothermal method without using extraneous additives by $Ca(OH)_2$ saturated solution reacted with CO_2 storage material (CO_2SM), which was obtained by absorbing CO_2 gas in a system containing equimolar ethylenediamine (EDA) and polyethylene glycol 400 (PEG). Specifically, homogeneous pure vaterite spheres were obtained by using 160 g/L CO_2SM solution at 100 °C and a reaction time of two hours. It is noteworthy that the EDA and PEG, which are released from CO_2SM, have dual functions as a CO_2 absorber and crystal regulator in the process of controlling the crystallization of $CaCO_3$ crystals.

Keywords: $CaCO_3$ microspheres; controllable synthesis; CO_2 storage material; CO_2 utilization

1. Introduction

Climate change, one of the most disturbing global environmental issues, primarily relates to continuously increasing CO_2 emission from burning fossil fuels [1–3]. Thus, it is necessary to develop CO_2 capture and utilization (CCU) technology to reduce CO_2 emission. Currently, there are four CO_2 separation technologies, consisting of pre-combustion decarburization, chemical chain combustion decarburization, oxygen-rich combustion decarburization, and post-combustion decarburization [4,5]. As an important CO_2 abatement technology, the post-combustion decarbonization captures CO_2 from the flue gas after combustion and reduces CO_2 in flue gases by about 80% [6,7]. Therefore, it has broad application prospects. In recent years, carbon capture and storage (CCS) and CCU processes have been developed to control CO_2 emission and resource recovery [8–12]. In particular, the preparation of $CaCO_3$ via the chelation of CO_2 has been studied extensively because $CaCO_3$, as one of the cheaper biological materials, has important applications in various fields [13–20]. There are four polymorphic phases that have been prepared as follows: calcite, aragonite, vaterite, and amorphous $CaCO_3$ (ACC) [21,22]. Calcite and aragonite $CaCO_3$ crystals are the most stable structures of thermodynamics, and vaterite would rapidly transform to aragonite and (or) calcite because it is the least thermodynamically stable [23]. Among them, the pure vaterite phase $CaCO_3$ crystals is studied most widely because it has a larger specific surface and porous nature that could improve mechanical properties when they are used as filler [24–26]. More importantly, it is challenging for the synthesis of stable vaterite when CO_2 is used as a direct raw chemical because the process is more dependent on the calcium source.

$CaCO_3$ powders are prepared by carbonization in industry. The morphology of $CaCO_3$ powders prepared by carbonization is disordered and the particle size is not uniform [27,28]. Recently, Mari et al. [13,19] captured CO_2 in aqueous solutions of methyldiethanolamine (MDEA) and 2-amino-2-methyl-1-propanol (AMP). At the same time, soluble calcium salts were added to the

system, and the CO_2 captured by amine in the system was further converted by the reaction with Ca^{2+} in the system to form $CaCO_3$ precipitation. However, $CaCO_3$ is easy to agglomerate, its morphology is disordered, and the size of particle is larger. Therefore, the preparation of $CaCO_3$ with fixed morphology, monodisperse, small particle size, and single crystal phase has become a hot spot in the research of $CaCO_3$ mineralization.

In the work, the polyethylene glycol 400 (PEG400) was added into ethylenediamine (EDA) to enhance the ability of the system absorbing CO_2, which formed CO_2 storage material (CO_2SM) (Figure 1). After that, the as-prepared CO_2SM was used to investigate the crystallization of $CaCO_3$ crystals via a simple hydrothermal reaction. Whereas EDA provided a high pH environment, polyethylene glycol (PEG) induced the formation of vaterite $CaCO_3$ crystals. Furthermore, the optimal synthesis conditions were identified by exploring the concentration of CO_2SM solution, reaction temperature, and reaction time. Specially, the stable pure vaterite phase $CaCO_3$ crystals in nature also could be prepared under experiment condition. It is anticipated that the result of this is significant for the indirect utilization of CO_2. The process integrates CO_2 capture and resource utilization, effectively utilizes CO_2, and generates value-added $CaCO_3$.

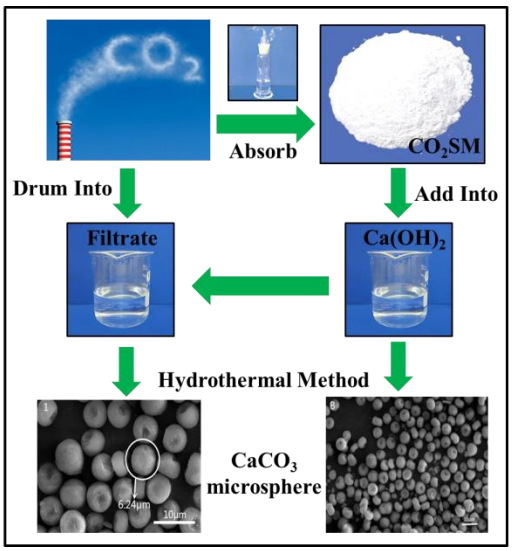

Figure 1. The preparing process of morphology controlled $CaCO_3$ micro-particles. The equimolar system ethylenediamine (EDA) + polyethylene glycol (PEG) reacted with CO_2 to obtain CO_2 storage material (CO_2SM), which was added into the $Ca(OH)_2$ solution to obtain $CaCO_3$ precipitate via the hydrothermal method. Subsequently, CO_2 was bubbled into filtrate before the addition of $Ca(OH)_2$ solution, and $CaCO_3$ particles with the same crystal phase were also recycled to obtain the same reaction conditions.

2. Experimental Section

2.1. Materials

The purity of EDA was 98%, which was provided by Yongsheng Fine Chemical Co., Ltd., Tianjin, China. The solid of $Ca(OH)_2$ was provided by Sinopharm Chemical Reagent Co., Ltd., Shanghai, China. PEG 400 with a molecular weight range of 380–420 g/mol, was analytical grade and was provided by the Beijing Reagent Company Co., Ltd., Beijing, China. The purity of compressed CO_2 was 99.999%, which was provided by the China Standard Things Center, Beijing, China. CO_2SM was obtained by capturing via the equimolar EDA + PEG400 system according to the previous study.

2.2. Synthetic Procedures

In line with a typical $CaCO_3$ preparing process, 1 g CO_2SM was added into a stainless steel reactor (the specifications of Teflon-lined is 100 mL), which was filled with 50 mL saturated $Ca(OH)_2$ solution. The reaction was controlled at 100 °C for 2 h, and then was cooled down until it reached room temperature. The mixture of precipitate and solution was separated by vacuum filtration, and it was washed at least three times by aqua distillate. The collected filter cake was dried at 120 °C for more than 4 h under vacuum.

2.3. Characterization

The morphology of $CaCO_3$ precipitates were observed by scanning electron microscope (SEM) and energy dispersive X-ray spectroscopy (Quanta FEG 650, Beijing, China), with an accelerating voltage of 20 kV. The crystal lattice spacing was observed by high resolution transmission electron microscope (HR-TEM; JEM-2100, Beijing, China), and the accelerating voltage was 200 kV. The X-ray diffractometer (XRD) was made in Germany from Siemens D/max-RB at 2θ = 5–80°, and the scanning rate was 0.05°/s (the mass of a sample was about 0.5 g), which used a powder with Cu Kα (λ = 1.5418 Å) radiation. The Fourier transform infrared spectroscopy (FTIR) technology was made in the USA by Nexus 670, and the CO_2SMs dispersed in KBr powder, with a resolution of 1 cm^{-1} from (4000 to 400) cm^{-1}. The thermogravimetric analysis (TGA) technology was made in Germany by Entzsch-Sta 449 and the samples were met with the heating rate of 5 °C min^{-1} (the mass of a sample was about 0.3–0.5 mg). The automatic surface area (BET method) and porosity analyzer (BJH model) was made in the USA by TristarII 3020 to obtain nitrogen adsorption-desorption data (the mass of a sample was about 2.0 g). The BET method and BJH model are depended on the Equations (1) and (2):

$$P/[V(P_0 - P)] = 1/(V_m \times C) + [(C - 1)/(Vm \times C)] \times (P/Po) \quad (1)$$

where P is nitrogen partial pressure, P_0 is adsorption temperature, nitrogen saturated vapor pressure, V is the actual adsorption amount of nitrogen on the sample surface, V_m is nitrogen monolayer saturated adsorption amount, C is constants related to the adsorption capacity of the sample

$$\ln \frac{P}{P_0} = \frac{2\gamma V_m}{rRT} \quad (2)$$

where P is the actual vapor pressure, P_0 is the saturated vapor pressure, γ is the surface tension, V_m is the molar volume of the liquid, R is the general gas constant, r is the radius of the droplet, T is the temperature.

The X-ray photoelectron spectroscopy (XPS) technology was made in the USA by ESCLAB-250Xi with a monochromatized Al Kα X-ray (hν = 1486.6 eV) operating at 150 W from (200 to 600) eV.

The percent molar content of calcite, vaterite, and aragonite in the precipitate was calculated by Equations (3) to (5) [29]:

$$X_A = \frac{3.157 \times I_A^{221}}{I_C^{104} + 3.157 \times I_A^{221} + 7.691 \times I_V^{110}}, \quad (3)$$

$$X_C = \frac{I_C^{104} \times X_A}{3.175 \times I_A^{221}}, \quad (4)$$

$$X_V = \frac{\left(I_C^{104} + 3.157 \times I_A^{221} + 7.691 \times I_V^{110}\right) \times 3.175 \times I_A^{221}}{\left(I_C^{104} + 3.157 \times I_A^{221} + 7.691 \times I_V^{110}\right) \times 3.175 \times I_A^{221}} - \frac{3.157 \times I_A^{221} \times 3.175 \times I_A^{221} - \left(I_C^{104} + 3.157 \times I_A^{221} + 7.691 \times I_V^{110}\right) \times I_C^{104} \times X_A}{\left(I_C^{104} + 3.157 \times I_A^{221} + 7.691 \times I_V^{110}\right) \times 3.175 \times I_A^{221}}. \quad (5)$$

The percent of molar content of only containing vaterite and calcite in the precipitate is calculated by Equations (6) and (7):

$$\frac{I_C^{104}}{I_V^{110}} = 7.691\frac{X_C}{X_V}, \tag{6}$$

$$X_V = \frac{\left(I_C^{104}+3.157\times I_A^{221}+7.691\times I_V^{110}\right)\times 3.175\times I_A^{221}}{\left(I_C^{104}+3.157\times I_A^{221}+7.691\times I_V^{110}\right)\times 3.175\times I_A^{221}} - \frac{\left(I_C^{104}+3.157\times I_A^{221}+7.691\times I_V^{110}\right)\times I_C^{104}\times X_A}{\left(I_C^{104}+3.157\times I_A^{221}+7.691\times I_V^{110}\right)\times 3.175\times I_A^{221}}, \tag{7}$$

where X_A, X_C, and X_V are the percent molar content of aragonite, calcite, and vaterite, respectively. The lattice planes of 221 ($I^{221}A$), 110 ($I^{110}V$), and 104 ($I^{104}C$) are due to aragonite, vaterite, and calcite.

3. Results and Discussion

Conventional protocols for regulating $CaCO_3$ polymorph mainly include variation of solvents [30], temperatures [31], and organic or inorganic additives [32]. Thus, the effect of three major factors were examined in the $CaCO_3$ crystallization process, such as CO_2SM concentration, temperature, and time.

3.1. Influences of CO_2SM Concentration

Various CO_2SM concentrations were examined to identify the influences of CO_2SM concentration on the preparation of $CaCO_3$ crystals, and the SEM photos of $CaCO_3$ crystals obtained at the CO_2SM concentration range of 20 to 160 g/L at 100 °C for 2 h are shown in Figure 2. Table 1 illustrates the preparation conditions and crystal composition of $CaCO_3$ crystals prepared with different CO_2SM concentrations, which indicated that the $CaCO_3$ crystals exhibited spherical-like shapes with an approximate particle diameter of 5–7 µm, at the same time, there was no obvious change in $CaCO_3$ crystal size with the increase of CO_2SM concentration. As listed in Table 1, the solution pH decreased gradually from 9.33 to 8.49 with increasing CO_2SM concentration. These results unambiguously revealed that the morphology of $CaCO_3$ crystals varied significantly with the increasing CO_2SM concentrations.

Table 1. The reaction conditions and polymorph composites of as-obtained $CaCO_3$ crystals under different CO_2SM concentrations at 100 °C for 2 h.

Sample [a]	Reaction Conditions [b] (CO_2SM g/L; pH)	Polymorph Composition [c] (%)		
		Calcite	Aragonite	Vaterite
A	20; 9.33	20.60	0	79.40
B	60; 8.75	0	0	100
C	95; 8.57	0	0	100
D	120; 8.53	0	0	100
E	160; 8.49	0	0	100

[a] The $Ca(OH)_2$ saturated liquid was 50 mL. [b] The unit of g/L was calculated by CO_2SM dispersed in $Ca(OH)_2$ saturated liquid. [c] Results were calculated by the X-ray diffractometer (XRD) patterns.

The XRD patterns of $CaCO_3$ crystals are shown in Figure 3. The main peaks of sample A (20 g/L) at 29.2° and 24.7° in the XRD patterns were assigned to the (104) face of calcite and the (110) face of vaterite, respectively [33], indicating the phase structure of the sample A was a mixture of calcite and vaterite, of which the CO_2SM concentration was 20 g/L. With the increasing CO_2SM concentration from 60 g/L to 160 g/L (samples B–E), the phase structures were pure vaterite because their characteristic peaks at 24.7° corresponded to the (110) face of vaterite, which is consistent with our previous work. The change trend above suggests that a high concentration of CO_2SM favors the formation of vaterite because of the low pH value of the medium [34–37], which probably favors the formation of the most thermodynamically stable polymorph—vaterite. In addition, the polymorph composition of $CaCO_3$ crystals are listed in Table 1.

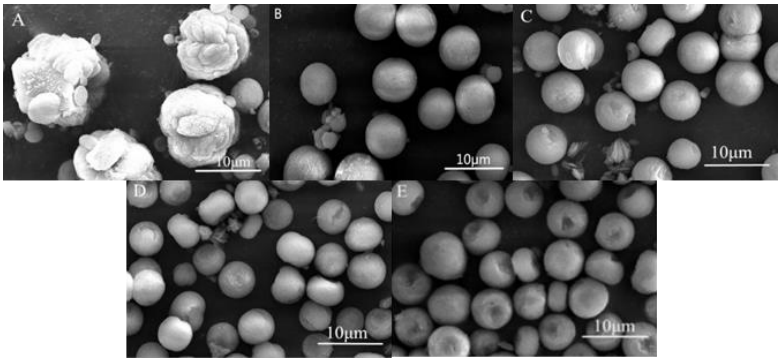

Figure 2. Scanning electron microscope (SEM) images of $CaCO_3$ crystals at different CO_2SM concentrations (g L^{-1}): **A**, 20; **B**, 60; **C**, 95; **D**, 120; and **E**, 160.

In general, there are four modes for the characteristic vibrations of the C–O bond of $CaCO_3$ crystals in FTIR spectra, which are the symmetric stretching mode, the out-of-plane bending mode, the doubly asymmetric stretching mode, and the doubly in-plane bending mode [38–40]. As shown in Figure 3b, two characteristic peaks at 875 and 711 cm^{-1} were observed, which was due to the υ_4 mode of calcite in the sample A. Meanwhile, the characteristic peak at 745 cm^{-1} was also observed, which corresponds to the υ_4 mode of vaterite. These results indicated that the crystal phase of sample A was a mixing crystal phase of calcite and vaterite. When the CO_2SM concentration was higher than 20 g/L, the characteristic peak at 711 cm^{-1} disappeared, indicating that the samples of B to E were pure vaterite phase. The analysis results of FTIR spectra and XRD spectra are unanimous.

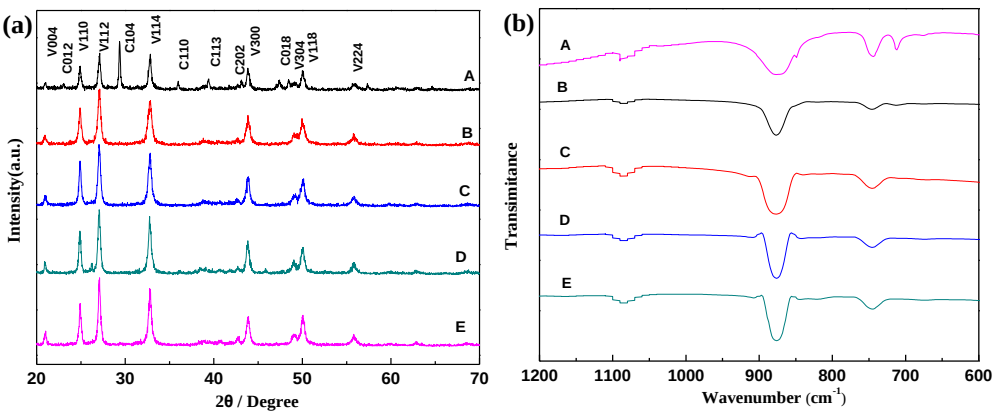

Figure 3. XRD patterns (**a**) and Fourier transform infrared spectroscopy (FTIR) spectra (**b**) of $CaCO_3$ crystals when the CO_2SM concentrations were as follows (g L^{-1}): A, 20; B, 60; C, 95; D, 120; and E, 160.

3.2. Influent of Reaction Temperature

Preparation conditions and crystal composition of $CaCO_3$ crystals at different reaction temperatures are listed in Table 2. It is known that the reaction temperature hardly influenced the morphology of $CaCO_3$ in Figure 4. In contrast, with increasing reaction temperature, the size of as-obtained $CaCO_3$ crystals increased firstly, and subsequently decreased. In the crystallization process, supersaturation was the driving force, as the supersaturation decreased with the rise of temperature and the nucleation rate slowed down, which made the growth rate slower and helped to increase the size of the crystals. The solubility of CO_2 in solution further decreased, and the content of CO_3^{2-} decreased with the further increase of temperature, which led to the formation of smaller particles and the smaller size of $CaCO_3$ crystals [15].

Table 2. The reaction conditions and polymorph composites of as-obtained $CaCO_3$ crystals under different temperatures in 160 g L^{-1} CO_2SM solution for 2 h.

Samples [a]	Preparation Conditions [b] (°C)	Polymorph Compost [c] (%)		
		Calcite	Aragonite	Vaterite
A	80	0	0	100
B	90	0	0	100
C	100	0	0	100
D	110	0	0	100
E	120	0	0	100

[a] The $Ca(OH)_2$ saturated liquid was 50 mL. [b] The unit of g/L was calculated by CO_2SM dispersed in $Ca(OH)_2$ saturated liquid. [c] Results were calculated by the XRD patterns.

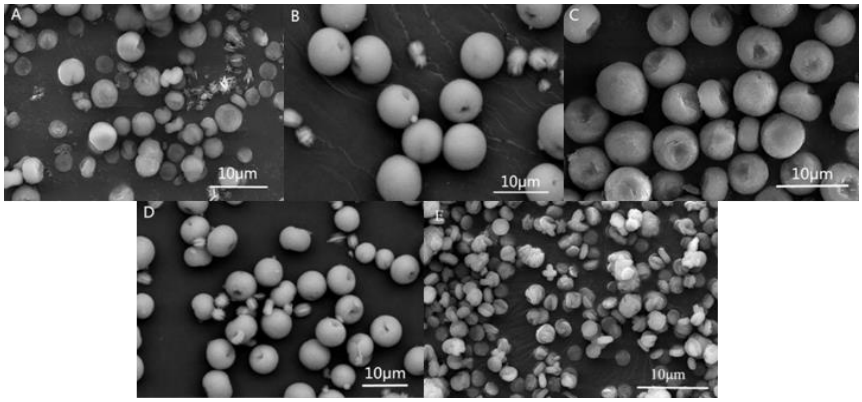

Figure 4. SEM images of $CaCO_3$ crystals under temperatures at 160 g L^{-1} CO_2SM solution for 2 h (°C): **A**, 80; **B**, 90; **C**, 100; **D**, 110; and **E**, 120.

The XRD patterns of $CaCO_3$ crystals were shown in Figure 5, which were obtained with the increasing temperature from 80 °C to 120 °C with 160 g/L CO_2SM for 2 h. As shown in Figure 5a, all samples were pure vaterite crystals because the main peak at 24.7° could be assigned to the 110 phase of vaterite. Furthermore, the polymorph composition of $CaCO_3$ crystals is listed in Table 2. The FTIR spectra in Figure 5 show that all the samples displayed three vibration bands at 1083, 875, and 745 cm^{-1}, which confirmed the presence of vaterite. These results suggest that there was no influence of reaction temperature on the phase.

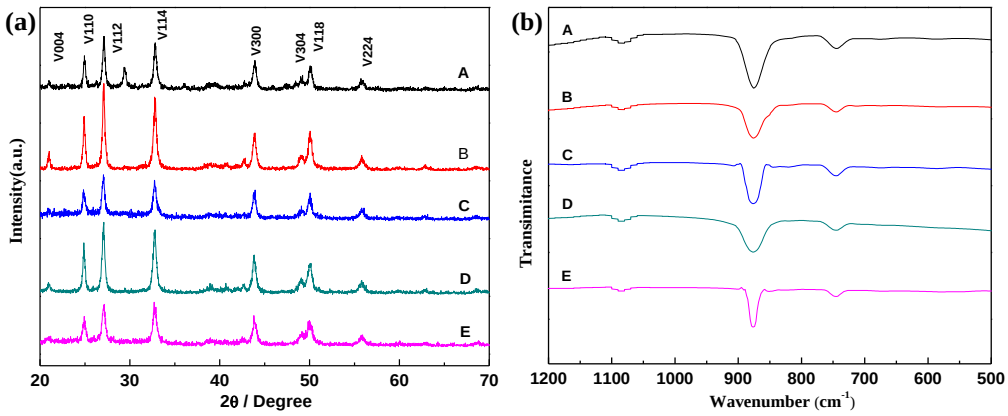

Figure 5. XRD patterns (**a**) and FTIR spectra (**b**) of $CaCO_3$ crystals with different reaction temperatures at 160 g L^{-1} CO_2SM solution for 2 h (°C): A, 80; B, 90; C, 100; D, 110; and E, 120.

3.3. Influents of Reaction Time

Preparation conditions and crystal composition of $CaCO_3$ crystals prepared with different reaction time are listed in Table 3. All the samples were spherical-like shapes, regardless of the reaction time in Figure 6. When the reaction time was extended, the microsphere of $CaCO_3$ gradually grew into defective spheres. As a result, the size of microspheres gradually decreased and became densely agglomerated. The reason may be that the nucleation rate of crystals is faster and the system is controlled by thermodynamics. In other words, the nucleation process of $CaCO_3$ particles was completed within 120 min, and then small particles began to agglomerate over time [15].

Table 3. The reaction conditions and polymorph composites of as-obtained $CaCO_3$ crystals with different reaction times at 100 °C and in 160 g L^{-1} CO_2SM solution.

Samples [a]	Preparation Conditions [b] (min)	Polymorph Compost [c] (%)		
		Calcite	Aragonite	Vaterite
A	60	0	0	100
B	120	0	0	100
C	240	0	0	100
D	360	0	0	100
E	480	0	0	100

[a] The $Ca(OH)_2$ saturated liquid was 50 mL. [b] The unit of g/L was calculated by CO_2SM dispersed in $Ca(OH)_2$ saturated liquid. [c] Results were calculated by the XRD patterns.

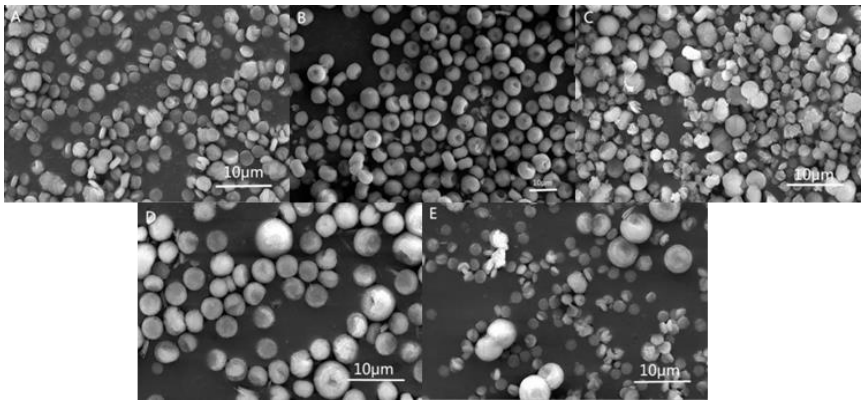

Figure 6. SEM images of $CaCO_3$ crystals with different times at 100 °C and 160 g L^{-1} (h): **A**, 1; **B**, 2; **C**, 4; **D**, 6; and **E**, 8.

The XRD patterns of $CaCO_3$ are shown in Figure 7, which were obtained at the reaction time ranging from 1 to 8 h and the reaction temperature of 100 °C with 160 g/L CO_2SM. As shown in Figure 7a, all the samples were pure vaterite crystals because their main peaks at 24.7° correspond to the 110 phase of vaterite. The polymorph composition of $CaCO_3$ crystals are listed in Table 3. The FTIR spectra in Figure 7b showed that all the samples displayed three vibration bands at 1083, 875, and 745 cm^{-1}, which confirmed the presence of vaterite.

It was suggested that the reaction time could affect the size of $CaCO_3$, which may have been because of the fast nucleation rate of $CaCO_3$, but it hardly impacted the morphology and crystal phase of $CaCO_3$ crystals.

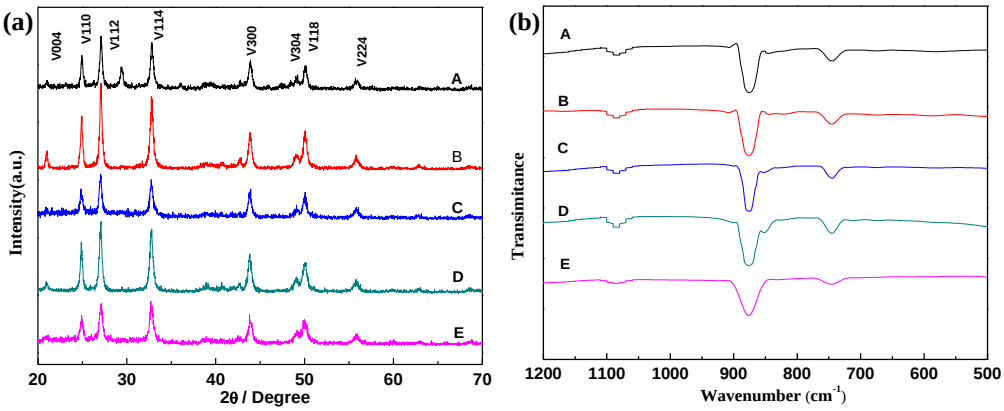

Figure 7. XRD patterns (**a**) and FTIR spectra (**b**) of $CaCO_3$ crystals with different times at 100 °C and 160 g L^{-1} (h): A, 1; B, 2; C, 4; D, 6; and E, 8.

3.4. Continuous Preparation of $CaCO_3$ Microspheres

The system consisting of equimolar EDA + PEG reacted with CO_2 to yield CO_2SM, which was added into $Ca(OH)_2$ solution to prepare $CaCO_3$ precipitate via the hydrothermal process. Then, the mixture of precipitate and solution was separated via vacuum filtration to obtain $CaCO_3$ powder and filtrate. Subsequently, CO_2 was bubbled into filtrate before the $Ca(OH)_2$ solution was added. The mixing solution was reacted at 100 °C and 160 g L^{-1} CO_2SM for 2 h. The process was recirculated five times. The characteristic peaks of products in FTIR were found at 877 and 745 cm^{-1}, as shown in Figure 8, which were ascribed to the CO_3^{2-} group of the vaterite phase, indicating that the uniform crystalline phase of $CaCO_3$ crystals could still be obtained after filtration.

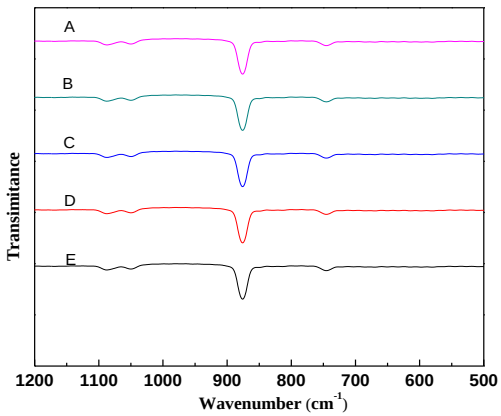

Figure 8. FTIR spectra of $CaCO_3$ crystals prepared with five cycles: A: firstly, B: secondly, C: thirdly, D: fourthly, and E: fifthly.

3.5. Possible Preapared Mechanism of as-Obtained $CaCO_3$ Microspheres

In this process (Figure 9), EDA would play pH-adjusting agent roles and PEG would play co-solvent roles in the growing process of $CaCO_3$ crystals [35–37,41]. The CO_2, which was released from the CO_2SM, transformed to CO_3^{2-} via the zwitterion mechanism, and at the same time, the CO_2SM produced RNH_3^+ and HCO_3^- at a higher pH (pH > 8) and subsequently abstracted H^+ by OH^- to produce CO_3^{2-}. On the other hand, the lone-pair electrons of O in -OH and N in NH_3 showed the strong electrostatic interactions between PEG and Ca ions in the mixing solution [35,42–45]. Therefore, the formation mechanism of $CaCO_3$ crystals was as follows:

$$RNH_2 + CO_2 + H_2O \rightarrow RNH_3^+ + HCO_3^-$$

$$RNH_2 + H_2O \rightarrow RNH_3^+ + OH^-$$

$$2RNH_3^+ + CaX_2 \rightarrow 2RNH_2 + Ca^{2+} + 2HX(X= Cl^-, NO_3^-, Br^-, CH_3COO^-)$$

$$PEG + Ca^{2+} \rightarrow PEG\text{-}Ca^{2+}$$

$$2PEG\text{-}Ca^{2+} + 2HCO_3^- + 2OH^- \rightarrow 2CaCO_3 + 2H_2O + 2PEG$$

The normal polymorph phase transformation of $CaCO_3$ is vaterite to calcite. The reverse phase transformation was observed in the systems as a result of the electrostatic interactions between surface layers containing two orientations of the CO_3^{2-} groups, and the calcium-rich surface promotes the crystallization of calcite.

As known by crystal growth kinetics, the growth rate of $CaCO_3$ crystals on one special direction might slow down due to the fact that the crystal adsorbs PEG and/or EDA on the same surface, which might lead to an isotropic growth of the crystal [46,47]. Thus, it is known that the concentration of PEG and EDA, which is directly related from CO_2SM, was of great significance in the $CaCO_3$ crystallization processes. The higher the CO_2SM concentration, the higher the EDA and PEG concentrations, which leads to more chances for collisions between different ions and the further formation of spherical particles.

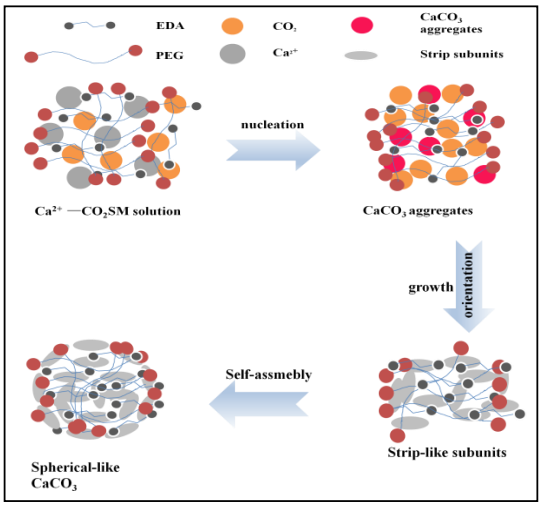

Figure 9. Possible prepared mechanism of as-obtained $CaCO_3$ microspheres.

3.6. Properties of $CaCO_3$ Microspheres

To further know the properties of the $CaCO_3$ microspheres, including the crystalline phase transformation and compositions, we further systematically investigated the spherical-like $CaCO_3$ micro-particles.

3.6.1. HR-TEM

Firstly, the lattice structure and the edge structure of $CaCO_3$ microspheres were analyzed by HR-TEM. As shown in Figure 10, there were the (112) plane (0.322 nm) and (114) plane (0.274 nm), which were attributed to the lattice of vaterite [48].

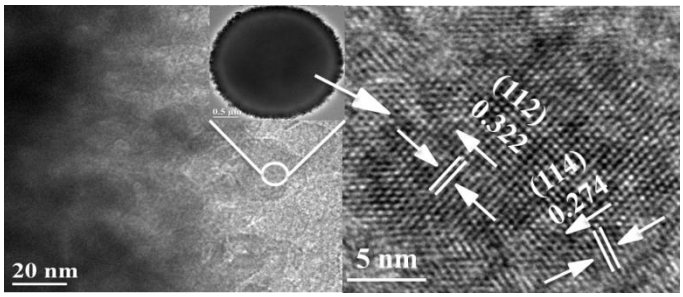

Figure 10. High resolution transmission electron microscope (HR-TEM) of as-obtained $CaCO_3$ microspheres.

3.6.2. TGA-DSC

TGA refers to the relationship between the mass of the sample to be measured and the temperature change under programmed temperature control. DSC refers to the relationship between the power difference (e.g. in the form of heat) input to the sample and the reference material and the temperature under programmed temperature control.

The spherical $CaCO_3$ microspheres were also analyzed by using TGA-DSC, and the result is shown in Figure 11. At the first stage of weight loss from the origin temperature at 592 °C, the weight loss rate of $CaCO_3$ microspheres was 4.83%, which is attributed to the volatilization of organic matters contained on the surface of $CaCO_3$ microspheres. At 790 °C, a very strong exothermic peak was observed in the DSC curve, which was caused by the thermal decomposition of $CaCO_3$ via the following reaction: $CaCO_3 \rightarrow CaO + CO_2\uparrow$ [49].

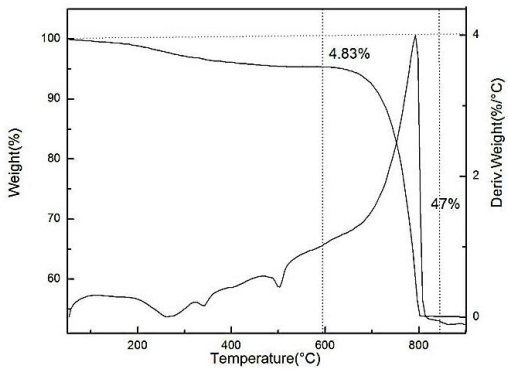

Figure 11. Thermogravimetric analysis curves of as-obtained $CaCO_3$ microspheres.

3.6.3. Surface Area and Pore Diameter

The N_2 adsorption–desorption curve and pore size distribution curve were also studied to evaluate the property of $CaCO_3$ microspheres. A specific surface area of $CaCO_3$ microspheres arrived at 152.04 m^2/g. Their average pore diameter and pore volume were determined to be 3.862 nm and 0.245 cc/g, respectively.

3.6.4. XPS and EDX

EDX refers to the determination of elements in samples according to the different characteristic X-ray wavelengths of different elements.

The microspheres of $CaCO_3$ were also analyzed by XPS and EDX, which are shown in Figures 12 and 13. From the EDX and XPS spectra, as-prepared $CaCO_3$ microspheres contained C, O, and Ca elements, but other elements were not observed, partially because of the low content of EDA and PEG in $CaCO_3$ microspheres.

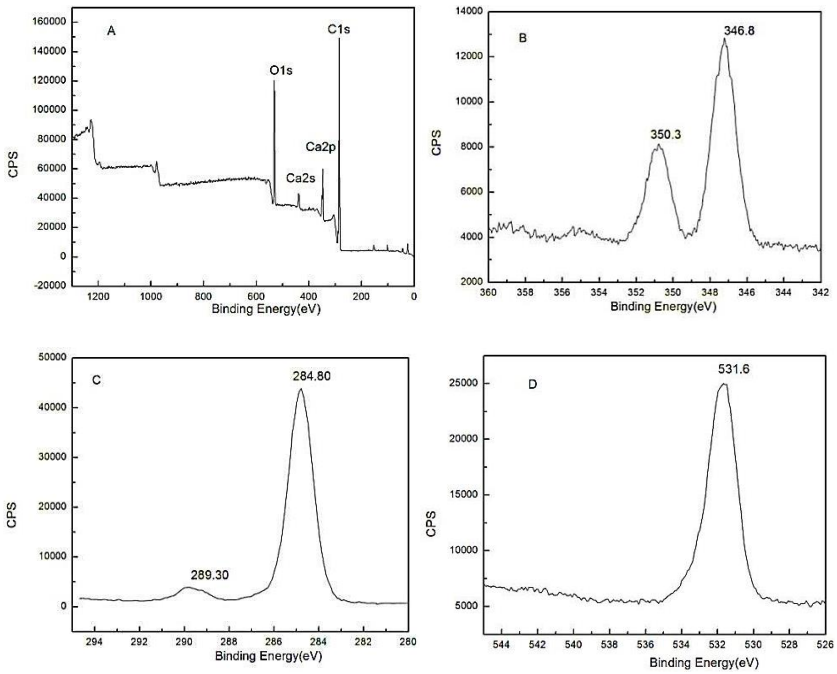

Figure 12. XPS spectra of as-obtained $CaCO_3$ microspheres. **A**: the total element; **B:** calcium element; **C**: carbon element; **D**: oxygen element.

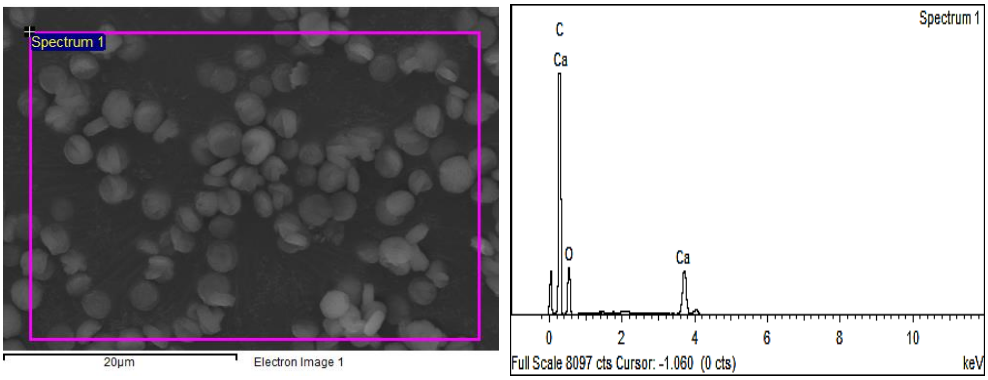

Figure 13. EDX results of as-obtained $CaCO_3$ microspheres.

4. Conclusions

CO_2SM, which was obtained by absorbing CO_2 via the EDA + PEG binary system solution, was mixed with $Ca(OH)_2$ to prepare $CaCO_3$ microspheres via hydrothermal reactions. The suitable preparation conditions were confirmed as follows: a CO_2SM concentration of 160 g/L, a reaction temperature of 100 °C, and a reaction time of 2 h. The as-prepared $CaCO_3$ crystals were homogeneous pure vaterite phase and the properties of $CaCO_3$ microspheres was confirmed. In addition, the uniform crystalline phase of $CaCO_3$ crystals could still be obtained after five times of cyclic preparation by filtrate. The as-obtained $CaCO_3$ by this method has high purity and uniform particle size, which may have a good application prospect in the paper industry.

Author Contributions: Conceptualization, H.G., Z.W. and J.Z.; methodology, X.M., Z.W. and J.Z.; software, X.M. and L.Z.; validation, H.G., Z.W. and J.Z.;; formal analysis, X.M., L.Z., F.S. and H.S.; investigation, X.M.; resources, H.G., Z.W. and J.Z.; data curation, H.G., Z.W. and J.Z.; writing—original draft preparation, X.M. and L.Z.; writing—review and editing, X.M., L.Z., F.S. and H.S.; visualization, X.M. and L.Z.; supervision, H.G., Z.W. and J.Z.; project administration, H.G., Z.W. and J.Z.; funding acquisition, H.G., Z.W. and J.Z.

Funding: We are grateful for the financial support provided by the National Natural Science Foundation of China (NSFC, 21666027), Key Laboratory of Coal-based CO_2 Capture and Geological Storage (Jiangsu Province, China University of Mining and Technology, 2016A06), the Natural Science Foundation of Inner Mongolia Autonomous Region (2016JQ02), the Program for Grassland Excellent Talents of Inner Mongolia Autonomous Region, the Inner Mongolia Science and Technology Key Projects, and Undergraduate Innovation Fund of Inner Mongolia University of Technology (2016).

Conflicts of Interest: There are no conflicts to declare.

Nomenclature

The checklist of nomenclature abbreviation:

Origin Vocabulary	**Abbreviations**
Calcium carbonate	$CaCO_3$
CO2-storage material	CO2SM
Carbon dioxide	CO_2
ethylenediamine	EDA
polyethylene glycol 400	PEG400
calcium hydroxide	$Ca(OH)_2$
CO2 capture and utilization	CCU
carbon capture and storage	CCS
scanning electron microscope	SEM
high resolution transmission electron microscope	HR-TEM
X-ray diffractometer	XRD
Fourier Transform infrared spectroscopy	FTIR
Thermogravimetric analysis	TGA
X-ray photoelectron spectroscopy	XPS

References

1. Barelli, L.; Bidini, G.; Gallorini, F. CO_2 capture with solid sorbent: CFD model of an innovative reactor concept. *Appl. Energ.* **2016**, *162*, 58–67. [CrossRef]
2. Li, B.; Duan, Y.; Luebke, D.; Morreale, B. Advances in CO_2 capture technology: A patent review. *Appl. Energ.* **2013**, *102*, 1439–1447. [CrossRef]
3. Luo, X.L.; Hu, J.H.; Zhao, J.; Zhang, B.; Chen, Y.; Mo, S. Multi-objective optimization for the design and synthesis of utility systems with emission abatement technology concerns. *Appl. Energ.* **2014**, *136*, 1110–1131. [CrossRef]
4. Li, B.H.; Zhang, N.; Smith, R. Simulation and analysis of CO_2 capture process with aqueous monoethanolamine solution. *Appl. Energ.* **2016**, *161*, 707–717. [CrossRef]
5. Cheung, O.; Bacsik, Z.; Liu, Q.; Mace, A.; Hedin, N. Adsorption kinetics for CO_2 on highly selective zeolites NaKA and nano-NaKA. *Appl. Energ.* **2013**, *112*, 1326–1336. [CrossRef]
6. Zheng, Q.H.; Farrauto, R.; Nguyen, A.C. Adsorption and methanation of flue gas CO_2 with dual functional catalytic materials: A parametric study. *Ind. Eng. Chem. Res.* **2016**, *55*, 6768–6776. [CrossRef]
7. Aliakbar, H.; Yang, J.H.; Tohidi, B.; Chuvilin, E.; Istomin, V. CO_2 capture by injection of flue gas or CO_2–N_2 mixtures into hydrate reservoirs: Dependence of CO_2 capture efficiency on gas hydrate reservoir conditions. *Environ. Sci. Technol.* **2018**, *52*, 4324–4330.
8. Gimeno, B.; Manuela, A.; Velasco, I.; Fernandez, J.; Blanco, S.T. Influence of SO_2 on CO_2 transport by pipeline for carbon capture and storage technology: Evaluation of CO_2/SO_2 capture. *Energ. Fuel.* **2018**, *32*, 8641–8657. [CrossRef]
9. Yin, W.; Alexis, G.; Iban, A.; Yang, C.Z.; Tarascon, J.M. Electrochemical reduction of CO_2 mediated by quinone derivatives: Implication for Li–CO_2 battery. *J. Phys. Chem. C* **2018**, *122*, 6546–6554. [CrossRef]
10. Niklas, A.; Leonard, J.M.; Annette, S.; Philip, V.; Andre, B. Selecting CO_2 sources for CO_2 utilization by environmental-merit-order curves. *Environ. Sci. Technol.* **2016**, *50*, 1093–1101.
11. Yuan, M.; Gao, G.; Hu, X.Y.; Luo, X.; Huang, Y.Q.; Jin, B.; Liang, Z.W. Premodified sepiolite functionalized with triethylenetetramine as an effective and inexpensive adsorbent for CO_2 capture. *Ind. Eng. Chem. Res.* **2018**, *57*, 6189–6200. [CrossRef]

12. Lee, M.G.; Kang, D.W.; Yoo, Y.; Jo, H.; Song, H.J.; Prk, J. Continuous and simultaneous CO_2 absorption, calcium extraction, and production of calcium carbonate using ammonium nitrate. *Ind. Eng. Chem. Res.* **2016**, *55*, 11795–11800. [CrossRef]
13. Vinoba, M.; Margandan, B.; Choi, S.Y.; Park, K.T.; Kim, H.J.; Jeong, S.K. Harvesting $CaCO_3$ polymorphs from in situ CO_2 capture process. *J. Phys. Chem. C* **2014**, *118*, 17556–17566. [CrossRef]
14. Du, H.C.; Steinacher, M.; Borca, C.; Huthwelker, T.; Murello, A.; Stellacci, F.; Amstad, E. Amorphous $CaCO_3$: Influence of the formation time on its degree of hydration and stability. *J. Am. Chem. Soc.* **2018**, *140*, 14289–14299. [CrossRef] [PubMed]
15. Boyjoo, Y.; Pareek, V.K. Synthesis of micro and nano-sized calcium carbonate particles and their applications. *J. Mater.Chem. A* **2014**, *2*, 14270–14288. [CrossRef]
16. Yan, F.; Jiang, J.G.; Li, K.M.; Tian, S.C.; Zhao, M.; Chen, X.J. Performance of coal fly ash stabilized, CaO-based sorbents under different carbonation–calcination conditions. *ACS Sustain. Chem. Eng.* **2015**, *3*, 2092–2099. [CrossRef]
17. Sacia, E.R.; Ramkumar, S.; Phalak, N.; Fan, L.S. Synthesis and regeneration of sustainable CaO sorbents from chicken eggshells for enhanced carbon dioxide capture. *ACS Sustain. Chem. Eng.* **2013**, *1*, 903–909. [CrossRef]
18. Sennoune, M.; Salvador, S.; Debenest, G. Impact of a CO_2-enriched gas on the decarbonation of CaCO3 and the oxidation of carbon in the smoldering process of oil shale semicoke. *Energ. Fuel.* **2012**, *26*, 391–399. [CrossRef]
19. Vinoba, M.; Margandan, B.; Grace, A.N.; Chu, D.H.; Nam, S.C.; Yoon, Y.; Yoon, S.H.; Jeong, S.K. CO_2 absorption and sequestration as various polymorphs of CaCO3 using sterically hindered amine. *Langmuir* **2013**, *29*, 15655–15663. [CrossRef]
20. Lee, S.; Sin, D.H.; Cho, K. $CaCO_3$ precipitation and polymorph forms during CO_2 sequestration from the atmosphere: Effects of the basic buffer components. *Cryst. Growth Des.* **2015**, *15*, 610–616.
21. Yao, Y.; Dong, W.; Zhu, S.; Yu, X.; Yan, D. Novel morphology of calcium carbonate controlled by poly(l-lysine). *Langmuir* **2009**, *25*, 13238–13243. [CrossRef] [PubMed]
22. Ihli, J.; Kulak, A.N.; Meldrum, F.C. Freeze-drying yields stable and pure amorphous calcium carbonate (ACC). *Chem. Commun.* **2013**, *49*, 3134–3136. [CrossRef] [PubMed]
23. Grasby, S.E. Naturally precipitating vaterite (μ-$CaCO_3$) spheres: Unusual carbonates formed in an extreme environment. *Geochim. Cosmochim. Acta* **2003**, *67*, 1659–1666. [CrossRef]
24. Hu, Z.; Deng, Y. Superhydrophobic surface fabricated from fatty acid-modified precipitated calcium carbonate. *Ind. Eng. Chem. Res.* **2010**, *49*, 5625–5630. [CrossRef]
25. Zhang, H.; Zeng, X.F.; Gao, Y.F. A facile method to prepare superhydrophobic coatings by calcium carbonate. *Ind. Eng. Chem. Res.* **2011**, *50*, 3089–3094. [CrossRef]
26. Wang, G.; Zhu, L.; Liu, H. Self-Assembled biomimetic superhydrophobic $CaCO_3$ coating inspired from fouling mineralization in geothermal water. *Langmuir* **2011**, *27*, 12275–12279. [CrossRef] [PubMed]
27. Huber, M.; Stark, W.J.; Loher, S. Flame synthesis of calcium carbonate nanoparticles. *Chem. Commun.* **2005**, 648–650. [CrossRef]
28. Hu, L.N.; Dong, P.F.; Zhen, G.W. Preparation of active $CaCO_3$ nanoparticles and mechanical properties of the composite materials. *Mater. Lett.* **2009**, *63*, 373–375. [CrossRef]
29. Chu, D.H.; Vinoba, M.; Bhagiyalakshmi, M.; Baekb, I.H.; Namb, S.C.; Yoonb, Y.; Kim, S.H.; Jeong, S.K. CO_2 mineralization into different polymorphs of $CaCO_3$ using an aqueous-CO_2 system. *RSC Adv.* **2013**, *3*, 21722–21729. [CrossRef]
30. Liu, L.; Jiang, J.; Yu, S.H. Polymorph selection and structure evolution of $CaCO_3$ mesocrystals under control of Poly(sodium 4-styrenesulfonate): Synergetic effect of temperature and mixed solvent. *Cryst. Growth Des.* **2014**, *14*, 6048–6056. [CrossRef]
31. Lu, S.Q.; Lan, P.Q.; Wu, S.F. Preparation of nano-$CaCO_3$ from phosphogypsum by Gas–Liquid–Solid reaction for CO_2 sorption. *Ind. Eng. Chem. Res.* **2016**, *55*, 10172–10177. [CrossRef]
32. Leukel, S.; Tremel, W. Water-Controlled crystallization of $CaCO_3$, $SrCO_3$, and $MnCO_3$ from amorphous precursors. *Cryst. Growth Des.* **2018**, *18*, 4662–4670. [CrossRef]
33. Sarkar, A.; Dutta, K.; Mahapatra, S. Polymorph control of calcium carbonate using insoluble layered double hydroxide. *Cryst. Growth Des.* **2013**, *13*, 204–211. [CrossRef]
34. Marcela, M.; Steinbach, C.; Aflori, M.; Simona, S. Design of high sorbent pectin/$CaCO_3$ composites tuned by pectin characteristics and carbonate source. *Mater. Des.* **2015**, *86*, 388–396.

35. Xu, X.Y.; Zhao, Y.; Lai, Q.Y.; Hao, Y.J. Effect of polyethylene glycol on phase and morphology of calcium carbonate. *J. Appl. Polym. Sci.* **2011**, *119*, 319–324. [CrossRef]
36. Jiang, J.X.; Ye, J.Z.; Zhang, G.W.; Gong, X.H.; Nie, L.H.; Liu, J.N. Polymorph and morphology control of $CaCO_3$ via temperature and peg during the decomposition of $Ca(HCO_3)_2$. *J. Am. Ceram. Soc.* **2012**, *95*, 3735–3738. [CrossRef]
37. Chuajiw, W.; Takatori, K.; Igarashi, T.; Hara, H.; Fukushima, Y. The influence of aliphatic amines, diamines, and amino acids on the polymorph of calcium carbonate precipitated by the introduction of carbon dioxide gas into calcium hydroxide aqueous suspensions. *J. Cryst. Growth* **2014**, *386*, 119–127. [CrossRef]
38. Lakkakula, J.R.; Kurapati, R.; Tynga, I.; Abrahamse, H.D.; Raichur, A.M.; Krause, R.W.M. Cyclodextrin grafted calcium carbonate vaterite particles: Efficient system for tailored release of hydrophobic anticancer or hormone drugs. *RSC Adv.* **2016**, *6*, 104537–104548. [CrossRef]
39. Ray, J.R.; Wong, W.; Jun, Y.S. Antiscaling efficacy of $CaCO_3$ and $CaSO_4$ on polyethylene glycol (PEG)-modified reverse osmosis membranes in the presence of humic acid: Interplay of membrane surface properties and water chemistry. *Phys. Chem. Chem. Phys.* **2017**, *19*, 5647–5657. [CrossRef]
40. Cheng, G.H.; Chai, Y.M.; Chen, J.; Chen, J.; Zhang, Q.; Ji, S.L.; Ou, L.L.; Yu, Y.T. Polystyrene–divinylbenzene based nano-$CaCO_3$ composites for the efficient removal of human tumor necrosis factor-α. *Chem. Commun.* **2017**, *53*, 7744–7747. [CrossRef]
41. Zhao, Y.Y.; Li, S.X.; Yu, L.; Liu, Y.H.; Wang, X.Q.; Jiao, J.J. The preparation of calcium carbonate crystals regulated by mixed cationic/cationic surfactants. *J. Cryst. Growth* **2011**, *324*, 278–283. [CrossRef]
42. Mihai, M.; Schwarz, S.; Doroftei, F.; Simionescu, B.C. Calcium carbonate/polymers microparticles tuned by complementary polyelectrolytes as complex macromolecular templates. *Cryst. Growth Des.* **2014**, *14*, 6073–6083. [CrossRef]
43. Qi, R.J.; Zhu, Y.J. Microwave-Assisted synthesis of calcium carbonate (vaterite) of various morphologies in water−ethylene glycol mixed solvents. *J. Phys. Chem. B* **2006**, *110*, 8302–8306. [CrossRef] [PubMed]
44. Li, Z.Q.; Xiong, Y.J.; Xie, Y. Selected-Control synthesis of ZnO nanowires and nanorods via a PEG-Assisted route. *Inorg. Chem.* **2003**, *42*, 8105–8109. [CrossRef] [PubMed]
45. El-Sheikh, S.M.; El-Sherbiny, S.; Barhoum, A.; Deng, Y. Effects of cationic surfactant during the precipitation of calcium carbonate nano-particles on their size, morphology, and other characteristics. *Colloids Surf. A* **2013**, *422*, 44–49. [CrossRef]
46. Guo, X.H.; Liu, L.; Wang, W.; Zhang, J.; Wang, Y.; Yu, S.H. Controlled crystallization of hierarchical and porous calcium carbonate crystals using polypeptide type block copolymer as crystal growth modifier in a mixed solution. *CrystEngComm* **2011**, *13*, 2054–2061. [CrossRef]
47. Geng, X.; Liu, L.; Jiang, J.; Yu, S.H. Crystallization of $CaCO_3$ mesocrystals and complex aggregates in a mixed solvent media using polystyrene sulfonate as a crystal growth modifier. *Cryst. Growth Des.* **2010**, *10*, 3448–3453. [CrossRef]
48. Ma, L.; Zhao, B.S.; Shi, H.H.; Sha, F.; Liu, C.; Du, H.; Zhang, J.B. Controllable synthesis of two CaO crystal generations: Precursors' synthesis and formation mechanisms. *CrystEngComm* **2017**, *19*, 7132–7145. [CrossRef]
49. Ligia, M.M.C.; Sakihama, J.; Salomao, R. Characterization of porous calcium hexaluminate ceramics produced from calcined alumina and microspheres of Vaterite (μ-$CaCO_3$). *J. Eur. Ceram. Soc.* **2018**, *38*, 5208–5218.